

# Relationship between global ocean mixing and mesoscale eddies

Guanghong Liao<sup>1</sup> and Zhi Liu<sup>2</sup>

<sup>1</sup>College of Oceanography, Hohai University, Nanjing, 210098, China

<sup>2</sup>Hohai University

September 14, 2022

## Abstract

Numerous studies have indicated that mesoscale eddies play an important role in diapycnal mixing and drive global water circulation. Although the relationships between eddy surface features and turbulent mixing have been discussed for individual cases of typical eddies, global studies cannot rely on ship-based microstructural measurements. Fine-scale methods have been developed, wherein either the vertical shear of velocity or density strain is used to estimate turbulent mixing. In this study, the turbulent dissipation rate was estimated using strain information from Argo floats trapped in eddies. Spatially averaged estimates revealed the global distribution patterns of the dissipation rates inside the eddies. In addition, the relationships between eddy features (polarity, radius, vertical extent, and aspect ratio) and turbulent dissipation rates were analyzed. Three main conclusions were made from this study. First, turbulent dissipation rates inside anticyclones were generally larger than those inside cyclones. Second, turbulent dissipation rates inside eddies are related to their vertical extent but not to their horizontal scale. For shallow eddies (with a vertical extent less than 250 m for cyclones and 300 m for anticyclones), the deeper the vertical extent, the larger the turbulent dissipation rate. Finally, the relationship between the eddy aspect ratio and turbulent dissipation rate was characterized by skewness. The average turbulent dissipation rate reached a maximum value when the cyclone aspect ratio was approximately 0.007; conversely, no maximum value was reached for anticyclones. This work establishes a correlation between eddy features and turbulent dissipation rates, which will help guide numerical simulations of mesoscale eddies.

## Hosted file

essoar.10512395.1.docx available at <https://authorea.com/users/539675/articles/599982-relationship-between-global-ocean-mixing-and-mesoscale-eddies>

# Relationship between global ocean mixing and mesoscale eddies

ZhiYing Liu<sup>1</sup>, GuangHong Liao<sup>1,2</sup>

1. Key Laboratory of Coastal Disaster and Protection (Hohai University), Ministry of Education, Nanjing, 210098, China;
2. Laboratory for Regional Oceanography and Numerical Modeling, Pilot National Laboratory for Marine Science and Technology, Qingdao, 266000, China

Corresponding Author:

GuangHong Liao

Email: [liaogh@hhu.edu.cn](mailto:liaogh@hhu.edu.cn)

## Abstract

Numerous studies have indicated that mesoscale eddies play an important role in diapycnal mixing and drive global water circulation. Although the relationships between eddy surface features and turbulent mixing have been discussed for individual cases of typical eddies, global studies cannot rely on ship-based microstructural measurements. Fine-scale methods have been developed, wherein either the vertical shear of velocity or density strain is used to estimate turbulent mixing. In this study, the turbulent dissipation rate was estimated using strain information from Argo floats trapped in eddies. Spatially averaged estimates revealed the global distribution patterns of the dissipation rates inside the eddies. In addition, the relationships between eddy features (polarity, radius, vertical extent, and aspect ratio) and turbulent dissipation rates were analyzed. Three main conclusions were made from this study. First, turbulent dissipation rates inside anticyclones were generally larger than those inside cyclones. Second, turbulent dissipation rates inside eddies are related to their vertical extent but not to their horizontal scale. For shallow eddies (with a vertical extent less than 250 m for cyclones and 300 m for anticyclones), the deeper the vertical extent, the larger the turbulent dissipation rate. Finally, the relationship between the eddy aspect ratio and turbulent dissipation rate was characterized by skewness. The average turbulent dissipation rate reached a maximum value when the cyclone aspect ratio was approximately 0.007; conversely, no maximum value was reached for anticyclones. This work establishes a correlation between eddy features and turbulent dissipation rates, which will help guide numerical simulations of mesoscale eddies.

**Key words:** Mesoscale eddy; Turbulent dissipation rate; Aspect ratio; Eddy features

## Introduction

Ocean mixing is generally divided into three types: molecular diffusion, vertical convection diffusion, and turbulent diffusion. Turbulent mixing is the primary form of mixing in the ocean (Thorpe, 2005) and plays an important role in determining the heat transport, water exchange, and vertical transport of dissolved substances at local and global scales (Whalen et al., 2012). In addition, turbulent mixing is accompanied by the transport of water components, which changes both horizontal and vertical density gradients and drives ocean circulation. Predictions of climate change are inseparable from predictions of ocean circulation (Vallis, 2006); thus, whether existing turbulent mixing parameterization schemes can meet the increasing spatial resolution of climate models should be addressed (Pope and Stratton, 2002). However, it is currently difficult to investigate the global distribution of turbulent mixing because of a lack of observations with sufficient spatial and temporal resolutions.

Based on the traditional one-dimensional convection-dissipation model, Munk (1966) proposed that the average ocean diffusion coefficient should reach  $O(10^{-4} \frac{m^2}{s})$  to maintain the observed ocean stratification structure. However, by using the microstructure profiler and chemical tracers, Gregg (1987) found that the average diffusion coefficient of the actual ocean was an order of magnitude less than the estimate of Munk at only  $O(10^{-5} \frac{m^2}{s})$ . These differences have attracted the attention of scientists, and observations and experiments have followed. Subsequent observations indicated that the turbulent diffusion coefficient has an obvious topographical dependence. The average diapycnal diffusivity observed by Polzin et al. (1996) in the sill, which is located in the equatorial Atlantic Ocean, is  $150 \times 10^{-4} m^2/s$ . In rough seabed topography, the diffusion coefficient may even exceed  $O(10^{-2} \frac{m^2}{s})$  (Carter and Gregg, 2002). Thus, the spatial and temporal variability of global turbulent mixing and its underlying mechanisms have remained a hot research topic.

To date, most turbulent mixing estimates have been based on specialized shear and microstructure observations with  $O(1 \text{ cm})$  resolution (Kunze et al., 2006). As turbulent mixing research progresses, observation technology can no longer meet the needs of the research community. Thus, scholars have begun using large-scale parameters to describe turbulent mixing. Henyey et al. (1986) first proposed a parameterization scheme to express the dissipation rate of turbulent kinetic energy by velocity shear and verified the validity of the method through numerical simulation. Subsequently, Wijesekera et al. (1993), no longer limited to using the velocity shear to represent turbulent mixing, attempted to calculate the turbulent dissipation rate using the stretching of the isobaric surface. Kunze et al. (2006) summarized and further popularized the aforementioned estimation methods, which are now widely used to estimate the turbulent dissipation rate and turbulent diffusion coefficient (detailed in Section 2).

Internal wave breaking is one of the fundamental dynamic mechanisms of turbulent mixing in the ocean and is the main mechanism of internal wave energy

dissipation. The mechanism of internal wave breaking is very complex, involving the nonlinear interaction between internal waves, sub-harmonic instability of nonlinear resonance, gravity instability, interaction between mesoscale eddies, and topography. Whalen et al. (2012) summarized four main factors affecting the turbulent dissipation rate: tidal energy, seafloor topography, near-inertial energy of the mixing layer, and mesoscale eddies. To study the relationship between tides and the turbulent dissipation rate, Peters (1997) carried out continuous observations in the Hudson Estuary for two days and found that ocean stratification was strong during neap tides, but the turbulent dissipation rate was small. Egbert and Ray (2003) discussed the relationship between each component tide and turbulent dissipation, and the results demonstrated that the M2 component tide caused the strongest dissipation of all the components. In addition, based on observations of and research on flat ocean basins and shelf slopes, Gregg et al. (2003) found that the turbulent dissipation rate increased as the roughness of the topography increased.

Mesoscale eddies also play an important role in turbulent mixing (Yang et al., 2014; Yang et al., 2019). Internal wave breaking caused by the interaction between eddies and topography is one of the most important mechanisms of turbulent mixing (Wunsch and Ferrari, 2004; Caulfield et al., 2017). Kunze and Sanford (2009) provided a theoretical solution for the propagation path of near-inertial internal waves in background shear flow by applying ray tracing theory and predicted that the anticyclone would strengthen turbulent mixing. However, global dissipation rates inside eddies are not available due to the lack of observations, making this prediction difficult to verify. Nevertheless, some scholars have conducted research on individual cases of eddies observed using a set of hydrographic and microstructural measurements (Sheen et al., 2015; Yang et al., 2019; Qi et al., 2020). Sheen et al. (2015) investigated the impact of a subsurface anticyclone in the Southern Ocean on local turbulent dissipation rates and found that turbulent dissipation was enhanced along the upper and lower eddy boundaries. Yang et al. (2019) found that turbulent dissipation was enhanced along the horizontal boundaries by observing a cyclone generated in the East China Sea and inferred that active sub-mesoscale processes at the edge of eddies enhance turbulent mixing. Qi et al. (2020) further observed an anticyclone with a complete trajectory using an underwater glider and concluded that the turbulence diffusivity at the posterior edge of the anticyclonic mesoscale eddy was an order of magnitude higher than that at the anterior side; the cause of this result was also inferred to be related to the generation and growth of sub-mesoscale motions at the posterior edge of the anticyclone. However, it is difficult to test such inferences with more examples of eddies, owing to the lack of efficient thermohaline observation methods. In recent years, an increasing number of Argo floats have been launched, making it possible to estimate the turbulent dissipation rate on a global scale. Wei et al. (2014) calculated the average diffusivity in 41 warm eddies and 27 cold eddies in the South China Sea based on Argo buoy data. The authors found that the average diffusivity in warm eddies was one order of magnitude higher than that in cold eddies in

the upper layer (from 100 to 500 m deep). In 2012, Whalen et al. discussed the spatiotemporal variability of turbulent dissipation on a global scale based on data acquired by the Argo floats. In another study by the authors, the amplitude of the seasonal cycle of turbulent mixing was enhanced in the presence of a strong and temporally uniform field of eddy kinetic energy (Whalen et al., 2018). To build off of previous reports, in this study, we attempted to establish a systematic relationship between turbulent mixing and eddy features based on Argo floats in the global ocean.

The remainder of this paper is organized as follows. In Section 2, we briefly describe the data and methods used for eddy detection and calculation of the turbulent dissipation rate. Section 3 presents the results of our analyses and a detailed discussion of the relationships between eddy features and turbulent dissipation rates inside the eddies. Finally, the study’s conclusions are presented in Section 4.

## Data and methods

### 2.1 Automated eddy detection

Eddies were identified from the most recent version of post-processed daily sea surface height anomaly (SSHA) data for the period from January 2002 to December 2017, which was provided by the Copernicus Marine Environment Monitoring Service (<http://marine.copernicus.eu/services-portfolio/access-to-products/>), with a spatial resolution of  $0.25^\circ \times 0.25^\circ$ . It is important to note that these gridded data have been smoothed to some degree, and both excessive and insufficient smoothing can cause misjudgment in eddy detection, especially for small-scale eddies. According to previous estimates (Chelton et al., 2011), the present SSH field has a feature resolution of only approximately 40 km. Relatively small eddies (radius less than 40 km) at high latitudes were mostly unresolved; therefore, SSHA data at latitudes higher than  $60^\circ$  were excluded from this study.

Automated eddy detection methods are basic tools for studying eddy characteristics from large datasets provided by satellite altimetry missions and numerical model simulations. Over the past 20 years, many studies have focused on the exploration of automated eddy detection methods, and many practical algorithms have been proposed (Chelton et al., 2007, 2011; Nencioli et al., 2010; Lily et al., 2011; Faghmous et al., 2015). These methods can usually be divided into two categories based on their application scenarios: the Lagrange and Euler methods. The former is primarily used to extract the oscillatory features of specific eddies in the regional sea (Lily et al., 2011), while the latter is more adaptable to large datasets and identifies eddies based on either their physical or geometrical characteristics. Euler methods based on physical criteria typically use expert-defined parameters to determine traces of the presence of an eddy, such as the Okubo–Weiss parameter (Petersen et al., 2013) and wavelet analysis

of the relative vorticity field (Doglioli et al., 2007). These methods can provide a clear picture of eddy evolution; however, they are also sensitive to noise. While spatial filtering is an effective tool for overcoming noise, it inevitably ignores some eddy signals. Such omissions add to the uncertainty in global ocean eddy monitoring studies (Souza et al., 2011). Euler methods based on geometrical characteristics identify eddies using physical parameters that exceed the chosen thresholds, such as sea surface temperature and SSHA. These methods involve searching for all possible eddy signals from the distribution of physical parameters and then removing false eddy signals by applying the constraints derived from the geometric characteristics of the eddy. Therefore, the main advantage of these methods is that they minimize the omission of eddy signals through a process of exclusion. However, using an empirical threshold to define the eddy boundary, as opposed to a physical one, inevitably introduces uncertainty. Despite these uncertainties, an improved geometric algorithm proposed by Faghmous et al. (2015) is able to recover 96.4% of the features identified by domain experts.

In this study, we used the automatic identification method proposed by Faghmous et al. (2015) based on gridded SSHA observations. After automatic detection,  $\sim 16.6$  million cyclones and  $\sim 16.2$  million anticyclones were identified from January 2002 to December 2017. On average, approximately 2840 cyclones and 2770 anticyclones were identified for each daily SSHA map, which is consistent with the results of Faghmous et al. (2015).

## 2.2 Characteristics of eddies

We defined eddy boundary using the peak azimuthal velocity to be consistent with the formula used for calculating the eddy aspect ratio. To obtain the peak azimuthal velocity, the eddy was decomposed into the azimuthal mean component and angular mode components in a polar coordinate system, with the eddy center as the pole (Liao et al., 2019):

$$h(r, \theta) = h_0(r) + \sum_{i=1}^{i=\infty} (a_i(r)\cos(i\theta) + b_i(r)\sin(i\theta)), \quad (1)$$

where the  $h_0(r)$  is the azimuthal mean component, representing the rotational symmetry of the eddy. The remaining components represent the interaction between the azimuthal mean component and Earth's vorticity field. From  $h_0(r)$ , the ideal geostrophic flow field of eddies can be obtained. The geostrophic flow field is then integrated along  $r$ , and the abscissa corresponding to the maximum value of the integrated geostrophic velocity is the eddy radius.

The eddy vertical extent cannot be obtained directly because of the lack of observations of the interior ocean. In this study, we inferred the eddy vertical extent using the following equation:

$$H = 2h_2 = \alpha R, \quad (2)$$

where  $h_2$  and  $R$  represent the eddy vertical half-height and radius, respectively, and  $\alpha$  is the eddy aspect ratio (defined as the vertical half-height over the eddy

radius). The most frequently cited relation for  $\alpha$  is  $\alpha = f/\bar{N}$ , where  $f$  is the Coriolis parameter and  $\bar{N}$  represents the average buoyancy frequency of the background field. This relationship is inferred from the quasi-geostrophic (QG) potential vorticity reported by Charney et al. (1971). However, the constraints under the QG equation are very restrictive, and Aubert et al. (2012) demonstrated that none of the meddies or laboratory eddies in their study satisfied these constraints. Hassanzadeh et al. (2012) derived a new relationship for the aspect ratio based on inviscid Boussinesq equations, given as:

$$\alpha^2 = \left(\frac{h_2}{R}\right)^2 = R_O(1 + R_O)f^2/(N_c^2 - \bar{N}^2), \quad (3)$$

where  $R_O$  is the Rossby number, defined as  $R_O = V_\theta/fR$  ( $V_\theta$  is the maximum value of the integrated geostrophic velocity mentioned above).  $\bar{N}$  and  $N_c$  represent the average buoyancy frequency of the background field and average buoyancy frequency at the eddy center, respectively. According to Equation (3), eddy aspect ratios strongly depend on the Rossby number,  $R_O$ , and buoyancy frequency at the eddy center,  $N_c$ . The Argo program provided approximately 2,000,000 profiles from January 2002 to December 2017, which can be used to calculate the average buoyancy frequencies,  $\bar{N}$  and  $N_c$ , and are freely available online (<http://www.argodatamgt.org/access-to-data/>). Aubert et al. (2012) validated Hassanzadeh et al.'s scaling law for  $\alpha$  using laboratory eddies and found good agreement between calculations and observations for typical eddy aspect ratios, such as those of Atlantic meddies, Jupiter's Great Red Spot, and Oval BA. More recently, Liu and Liao (2021) calculated the eddy aspect ratio in the global ocean and found a marked improvement in the magnitude of the aspect ratio in middle-high latitudes ( $>30^\circ$ ) over previously proposed scaling laws.

### 2.3 Calculating the turbulent dissipation rate inside eddies

We used the strain method originating from fine-scale parameterizations to estimate diapycnal mixing. This method was developed by Kunze et al. (2006) based on previous studies (Gregg, 1989; Wijesekera et al., 1993). The Argo program provides the temperature and salinity profiles required by the strain method. The Argo profiles were subjected to preliminary quality control by the Argo data center, and data flagged as good were used in our analysis. We further removed the mixed layer and areas of low stratification, as described by Whalen et al. (2012). The remaining profiles were divided into 250-m, half-overlapping segments starting from the bottom of each profile. The dissipation rate,  $\varepsilon$ , for each segment was calculated as follows:

$$\varepsilon = \varepsilon_0 \frac{\bar{N}^2}{N_0^2} \frac{\langle \xi_z^2 \rangle}{\langle \xi_{zGM}^2 \rangle} h(R_\omega) L(f, N), \quad (4)$$

where  $\xi_z = (N^2 - N_{\text{fit}}^2)/\bar{N}^2$  is the strain,  $N$  is the buoyancy frequency derived from the Argo profiles,  $\bar{N}$  is the vertically averaged buoyancy frequency of the segment, and  $N_{\text{fit}}^2$  is a quadratic fit of the buoyancy frequency.  $\varepsilon_0 = 8 \times 10^{-10} \text{ m}^2 \bullet \text{s}^{-2}$  and  $N_0 = 5.24 \times 10^{-3} \text{ rad} \bullet \text{s}^{-1}$  are reference values from

the Garrett–Munk (GM) model (Garrett and Munk 1975; Cairns and Williams 1976). To quantify the strain variance  $\langle \xi_z^2 \rangle^2$ , a linear fit was removed, and each strain segment was spatially Fourier-transformed for the strain spectra.  $\langle \xi_z^2 \rangle^2$  was calculated by integrating the strain spectra from the minimum wavelength to the maximum wavelength (50 and 300 m, respectively). The integration range can be adjusted for each Argo profile to avoid errors caused by instrument noise and removal of the linear fit (Kunze et al., 2006). The corresponding value from the GM model,  $\langle \xi_{z\text{GM}}^2 \rangle^2$ , was integrated over the same wavenumber range as  $\langle \xi_z^2 \rangle^2$ . The term  $h(R_\omega)$  accounts for the aspect ratio and frequency content of the internal wave field, expressed as follows:

$$h(R_\omega) = \frac{1}{6\sqrt{2}} \frac{R_\omega(R_\omega+1)}{\sqrt{R_\omega-1}}, \quad (5)$$

where  $R_\omega$  represents the shear-to-strain variance ratio. For a single wave,  $R_\omega$  depends on the velocity, and for the GM frequency spectrum,  $R_{\omega\text{GM}} = 3$ . The GM value  $R_\omega = R_{\omega\text{GM}} = 3$  was chosen as a reasonable estimate of  $R_\omega$  for the upper 2,000 m because of the lack of velocity observations (Kunze et al., 2006; Whalen et al., 2012). The term  $L(f, N)$  in equation (4) contains latitude dependence (Gregg et al., 2003), as follows:

$$L(f, N) = \frac{f \operatorname{arccosh}(\frac{N}{f})}{f_{30} \operatorname{arccosh}(\frac{N}{f_{30}})}, \quad (6)$$

where  $f$  is the Coriolis parameter and  $f_{30}$  is the Coriolis frequency at  $30^\circ$ . According to equation (2), the value  $L(f, N)$  at the equator is much smaller than that at mid-latitudes and  $L = 1$  at  $30^\circ$ , which is consistent with the result of a previous study on turbulent dissipation rates (Whalen et al., 2012).

In summary, we chose to use the strain method rather than the shear method given the lack of velocity observations. A software tool (based on both the strain method and the shear method) for estimating diapycnal mixing was developed previously, and the code is available from the IMAS (Institute for Marine and Antarctic Studies) technical report (Meyer et al., 2014). Finally, the turbulent dissipation rate  $\varepsilon$ , derived from Argo profiles ranging from  $10^{-12} \text{ W} \bullet \text{ kg}^{-1}$  to  $10^{-8} \text{ W} \bullet \text{ kg}^{-1}$ , and the logarithm of the dissipation rate ( $\log_{10} \varepsilon$ ) were used to more simply describe the intensity of diapycnal mixing in the subsequent analysis.

## 2.4 Synthetic analysis

The synthesis method used in this study assumes that the turbulent dissipation rates inside different eddies share similar distribution characteristics, that is, the eddies are barotropic. Based on the eddy detection results, the positions of the Argo floats were matched with eddy centers. The Argo floats trapped inside the eddies were selected for synthetic analysis. Briefly, we transferred all Argo floats trapped in different eddies into a normalized eddy, which behaved as a standard circle. The positions of the Argo floats were rearranged according to their positions relative to the eddy centers. The radius of the normalized eddy

was divided into 10 segments, and the variation in turbulent dissipation rates at different distances from the eddy center was obtained by averaging the turbulent dissipation rate at each segment. The specific steps are described below.

First, only the Argo profiles trapped inside the eddies were required in this study. An Argo float could be used if it satisfied both of the following constraints: (1) the time interval between the Argo floats and the eddy was no more than two days, and (2) the distance between the Argo floats and the eddy center was less than the eddy radius. Illustrative examples of Argo floats collected inside eddies are shown in Fig. 1. Using this method, approximately 0.54 million Argo profiles, trapped inside approximately 0.42 million eddies, were selected for synthetic analysis. Detailed statistics on the quantities of Argo floats trapped inside an eddy are presented in Table 1. The coordinates of the Argo floats were transformed into an eddy-centered polar coordinate system normalized by the eddy radius. In this system, an Argo float located precisely at the eddy center would have the coordinates ( $\rho = 0$ ), whereas an Argo float located precisely at the boundary of an eddy would have the coordinates ( $\rho = 1$ ). For example, in Fig. 1, the Argo float  $A_1$  is 28 km away from the eddy center C, and the eddy radius R is 42 km; thus,  $A_1$  has coordinates ( $\rho = 0.67$ ). Finally, the normalized radius was divided into 10 segments (Fig. 2). All Argo floats located in each segment were collected, the quantities of which are presented in Fig. 2.

In summary, based on the assumption that turbulent dissipation rates inside different eddies share similar distribution characteristics, all Argo floats trapped in different eddies were transferred into a normalized eddy for synthetic analysis. The average turbulent dissipation rate inferred from these Argo profiles indicates the distribution of the turbulent dissipation rate along the eddy radius.

## Results

### 3.1. Variability of turbulent dissipation rates along eddy trajectories

In Section 2, a large number of Argo floats trapped inside eddies (as determined by altimeter observations) were collected to calculate turbulent dissipation rate profiles. However, it was difficult to investigate the evolution of the turbulent dissipation rate along eddy trajectories owing to the temporal and spatial discontinuity of the Argo data. Only 676 eddy trajectories (331 cyclone trajectories and 345 anticyclone trajectories) sustained Argo float observations throughout their lifetimes. Among them, an anticyclonic and a cyclonic trajectory were selected as examples to illustrate the variability of the turbulent dissipation rate along eddy trajectories.

The anticyclone was generated on January 5, 2017, and declined on April 24, 2017, persisting for 110 days. The average radius of the anticyclone was 67.4 km. An Argo float moving along the anticyclone was selected and provided 12 valid profiles. The positions of the observation stations and the anticyclone

trajectory are shown in Fig. 3a. The dissipation rate profiles inferred from the 12 observation sites are shown in Fig. 3b and Fig. 3c. As shown in Fig. 3c, the average dissipation rate profile inside the anticyclone was divided into three segments centered at depths of 200–400 m, 400–1200 m, and 1200–1800 m. Between 200 and 400 m, the average dissipation rate tended to decrease rapidly from  $O(10^{-7})$  to  $O(10^{-9})$  in just 200 m. This was assumed to represent the continuation of the turbulent kinetic energy dissipation in the mixed layer. Between 400 and 1200 m, the average dissipation rate tended to decrease slowly from  $O(10^{-9})$  to  $O(10^{-10})$  in 800 m. Below 1200 m, the average dissipation rate was stable at  $O(10^{-10})$ . Extreme values for 1200–1600 m are shown in Fig. 3c and are also evident in Fig. 3b (highlighted by the black dotted box). Sheen et al. (2015) used a number of observations to investigate a subsurface Southern Ocean eddy and concluded that the presence of the eddy enhanced dissipation rates near the upper and lower boundaries of the eddy, causing extreme turbulent dissipation rate values in the inner ocean. Therefore, although it was difficult to estimate the vertical extent from the aspect ratio of the anticyclone due to the lack of observations at the anticyclone center, the vertical extent at the observation sites could be estimated based on the turbulent dissipation rate profiles. The extreme values observed near the 1800-m depth were considered to be related to bottom roughness, which was also mentioned in Whalen et al. (2012).

The cyclone was generated on January 31, 2004, and declined on April 6, 2017, persisting for 67 days. The average radius of the cyclone was 59 km. An Argo float moving with the cyclone provided eight valid profiles (Fig. 4a). Maps showing the turbulent dissipation rate profiles inferred from the eight observation sites are presented in Fig. 4b and Fig. 4c. The average turbulent dissipation rate profile inside the cyclone shared a distribution pattern similar to that inside the anticyclone and was also divided into three segments, which were centered at depths of 200–350 m, 350–1100 m, and 1100–1600 m. Between 200 and 350 m, the average dissipation rate tended to decrease rapidly from  $O(10^{-8})$  to  $O(10^{-12})$  in just 150 m. The average dissipation rate then decreased more slowly from  $O(10^{-12})$  to  $O(10^{-14})$  between 350 and 1100 m. Below 1100 m, the dissipation rate remained stable at  $O(10^{-14})$ . Two distinct extreme segments were observed in the turbulent dissipation rate profiles in Fig. 4c between 700–1000 m and 1200–1600 m (highlighted by the black dotted box). The max-min of the turbulent dissipation rates between these two segments were large (from  $O(10^{-12})$  to  $O(10^{-16})$ ; Fig. 4b). This large difference indicates that the turbulent mixing process inside the cyclone is complex. Owing to the lack of observations, it was difficult to study whether dynamic processes occurring at the cyclone bottom boundary dominate the extreme segments between 700–1000 m. As shown in Fig. 4b, the extreme values near 1600 m were clearly visible from day 10 and extended upward; thus, we considered the extreme values between 1200–1600 m to be related to bottom roughness, which is consistent with Whalen et al. (2012).

In summary, eddy polarity plays an important role in turbulent mixing inside

eddies. Owing to a lack of observations, it is difficult to analyze the dynamic mechanisms of the variance; therefore, in the following sections, we will summarize the relationships between eddy characteristics (namely polarity, radius, vertical extent, and aspect ratio) and the turbulent dissipation rate using statistical methods.

### 3.2. Spatial and seasonal variability of turbulent dissipation rates

Fig. 5 shows the vertical profile of the average dissipation rate inside the eddies. The dissipation rate is primarily related to variations in buoyancy frequency (Equation (4)); therefore, the average dissipation rate decreases with depth. Three different patterns of average dissipation rates with depth are shown in Fig. 5. Between 200 and 600 m, the average dissipation rate decreased rapidly. Between 600 and 1000 m, the average dissipation rate exhibited a significant maximum before decreasing with depth below 1000 m. However, compared with the decreasing trend observed for 200–600 m, the average dissipation rate decreased more slowly below 1000 m and was accompanied by a small disturbance. Based on these trends, we focused our analysis on three segments centered at depths of 200–600 m, 600–1000 m, and 1000–2000 m. Notably, the variance of the average dissipation rate decreased with depth, indicating that the mechanism affecting the turbulent dissipation rate in the upper layer was more complex than that in the bottom layer. The spatial distribution of the turbulent dissipation rate inside the eddies for segments centered between the abovementioned depths is shown in Fig. 6. The turbulent dissipation rate is closely related to the tidal energy, near-inertial energy, mesoscale kinetic energy, roughness topography, and proximity to the equator (Whalen et al, 2012), thereby exhibiting significant spatiotemporal heterogeneity. Some locally intensified mixing dissipation over regions of rough topography is related to breaking internal waves, which are generated by local interactions between the geostrophic or tidal flow and topography (Kunze et al., 2006; Whalen et al, 2012). Heightened mixing occurs in the strong Antarctic Circumpolar Current (ACC) and West Boundary Current (WBC) regions, such as the Kuroshio and Gulf streams. These are also regions of active mesoscale eddies with high mesoscale kinetic energy (Chang et al., 2015; He et al., 2019) and strong near-inertial energy (Chaigneau et al., 2008; Guo et al, 2020). In this study, we observed regional intensification of the turbulent dissipation rate inside the eddies in the upper layer (200–600 m), as shown in Fig. 6a. The mean dissipation rate at the depth interval of 600–1000 m also exhibited high values in both the ACC and WBC regions.

We also analyzed the seasonal distribution of the turbulent dissipation rate inside the eddies (Fig. 7). In the upper layer (200–600 m), the turbulent dissipation rates inside the eddies during winter and spring were generally larger than those during summer and autumn; this seasonal variation was specific to the upper 600 m. Similar seasonal variations were previously proposed by Whalen et al. (2012), who showed that the seasonal variation in turbulent

mixing is consistent with the seasonal variations in surface wind stress.

### 3.3. Eddy polarity and turbulent dissipation rate

Kunze et al. (1985) proposed that an anticyclone is favorable for the downward propagation of near-inertial energy. Subsequent studies have also shown that anticyclones can promote turbulent mixing (Zhai et al., 2005; Kunze et al., 2006). In this section, statistical methods based on approximately 0.42 million eddy samples were used to reveal differences in turbulent dissipation rates inside cyclones and anticyclones.

The eddy samples were divided into two groups based on polarity: approximately 0.21 million cyclones and 0.21 million anticyclones. The distribution of the turbulent dissipation rate inside the eddies between the three depth segments (200–600 m, 600–1000 m, and 1000–2000 m) is shown in Fig. 8. In the upper layer (200–600 m), the turbulent dissipation rates inside anticyclones are larger than those inside cyclones, especially in both the ACC and WBC regions. In the Kuroshio region, a larger dissipation rate was observed between 600 and 1000 m. The ratio of turbulent dissipation rates averaged over a  $1^\circ$  square bin inside the anticyclones and cyclones ( $\frac{\log_{10}(\epsilon_{\text{cyclone}})}{\epsilon_{\text{anticyclone}}}$ ) was used to measure the magnitude difference in the turbulent dissipation rate. The zonal average of the global ratio data was obtained, and the statistical results are shown in Fig. 8g–i. Between the three depth segments, the number of points with a ratio less than 0 was more than 40, which was three times larger than the number of points with a ratio greater than 0, even five times between 200 and 600 m. Therefore, we concluded that, in the upper 2000 m, the turbulent mixing intensity inside anticyclones was generally stronger than that inside cyclones.

### 3.4. Eddy radius and turbulent dissipation rate

Eddy radius is related to the rotation rate and background stratification. There may be differences between the turbulent mixing process inside and outside the eddies, and the turbulent dissipation rates inside eddies with different radii may also differ. Therefore, the following two issues were considered: (1) the relationship between the turbulent dissipation rate and the distance from the eddy center in a range of sea areas (twice the radius from the eddy center), and (2) the relationship between the turbulent dissipation rate inside the eddies and at the eddy radius. Consideration (1) can be further broken down into two parts: (1a) the distribution of the turbulent dissipation rate inside the eddies, and (1b) the difference between the turbulent dissipation rate inside and outside the eddies.

To investigate consideration (1a), we analyzed approximately 0.21 million cyclones and 0.21 million anticyclones, which were the same as the samples in Section 3.3. Given the lack of spatially continuous observations, it was difficult to determine the azimuthal anisotropy of the dissipation rate inside the eddies;

therefore, we instead focused on the relationship between the turbulent dissipation rate and the distance from the eddy center. All Argo floats trapped in the eddies were collected, and their positions relative to the eddy centers were recorded within the normalized radius (detailed in Section 2.4). The relationship between the turbulent dissipation rate inside the eddies and the normalized radius of the eddies is shown in Fig. 9. The number of Argo floats in each segment was greater than 1800, adding credibility to the results (also shown in Fig. 2). The turbulent dissipation rate at the eddy center (normalized radius less than 0.2) was higher than that in the remaining region inside the eddy for both cyclones and anticyclones. The turbulent dissipation rate in the remaining region inside the cyclone did not vary with the distance from the eddy center, and the average turbulent dissipation rate remained almost constant. Conversely, the turbulent dissipation rate inside the anticyclone decreased with increasing distance from the eddy center. In addition, the decrease in the dissipation rate inside the anticyclone was the smallest at 200–600-m depths.

To address consideration (1b), the Argo floats located within a specific sea area (more than one and less than two times the radius from the eddy center) were used to calculate the turbulent dissipation rate outside the eddies; in total, 1.1 million profiles for cyclones (Fig. 10) and 1.4 million profiles for anticyclones (Fig. 11) were included. From the spatial distribution map, the distribution of turbulent dissipation rates outside the eddies (for cyclones in Fig. 10a–c and for anticyclones in Fig. 11a–c) and inside the eddies (shown in Fig. 8) shared a similar pattern. Heightened mixing was observed in the ACC and WBC regions both inside and outside the eddies. The ratio of turbulent dissipation rates inside the eddies to that outside the eddies ( $\frac{\log_{10}(\epsilon_{\text{outside}})}{\epsilon_{\text{inside}}}$ ) was used to describe the difference more clearly (Fig. 10d–f and Fig. 11d–f). When the ratio was greater than 0, the turbulent dissipation rate outside the eddies was greater than that inside the eddies, and vice versa. The zonal average ratio of the cyclones is shown in Fig. 10d–f. In the upper layer (200–600 m), the number of points with a ratio greater than 0 was 44, which was much larger than the number of points with a ratio less than 0 (14). Between 600 and 2000 m, the number of points greater than 0 was 34, compared to 23 points less than 0. This indicates that the dissipation rate outside the cyclones was greater than that inside the eddies, which is consistent with the results of the eddy case located in the Northern South China Sea (Yang et al., 2019). Adams et al. (2017) presented high-resolution observations across the ACC as a cyclone formed in the Scotia Sea and found that enhanced mixing was prompted by active sub-mesoscale processes; thus, our results can be attributed to the fact that active sub-mesoscale processes at the cyclone boundaries, related to surface wind, enhanced turbulent mixing outside the cyclones. The zonal average ratio of the anticyclones is shown in Fig. 11d–f. Between the three depth segments, the number of points with a ratio less than 0 was approximately twice the number of points with a ratio greater than 0. These results indicate that the turbulent dissipation rate inside eddies is generally larger than that outside eddies and suggest that turbulent mixing can be enhanced by anticyclones.

In summary, we found that the turbulent mixing at the eddy center (normalized radius less than 0.2) was enhanced, irrespective of whether inside cyclones or anticyclones. Additionally, the turbulent dissipation rates in the remaining regions inside cyclones were evenly distributed, and those outside cyclones were larger than those inside cyclones due to active sub-mesoscale processes. Lastly, the turbulent dissipation rates inside anticyclones decreased with distance from the eddy center, and the average turbulent dissipation rate inside anticyclones was larger than that outside anticyclones.

The abovementioned samples was also used to investigate consideration (2). The variation in turbulent dissipation rates inside the eddies with changes in eddy radii is shown in Fig. 12. The turbulent dissipation rate inside eddies with radii greater than 220 km fluctuated significantly, which may be a consequence of the relatively small number of eddy samples (less than 100). In conclusion, eddy radius did not influence the turbulent dissipation rate inside the eddies.

### 3.5 Eddy vertical extent and turbulent dissipation rate

The vertical extent of eddies is a parameter that describes the vertical morphological characteristics of eddies. Internal wave breaking caused by the interaction between mesoscale eddies and topography in the open ocean is one of the most important mechanisms of turbulent mixing (Caulfield et al., 2017). Therefore, differences in vertical extent may correlate with differences in turbulent dissipation rates.

According to Equation (1), the Temperature/Salinity (T/S) profiles located at the eddy center (identified within 14 km from the eddy center) are needed to calculate the vertical extent of the eddies. Therefore, the data were screened to include 8688 eddies (4284 cyclones and 4404 anticyclones) with vertical extent ranges from 100 to 4000 m (Liu et al., 2020). Only 672 eddies extended more than 2000 m, accounting for 7.7%. Thus, samples with vertical extents greater than 2000 m were removed to be consistent with the depth of the turbulent dissipation profiles. After filtering, 8016 eddies (4099 cyclones and 3917 anticyclones) were included for analysis.

Maps showing the relationship between the eddy vertical extent and average turbulent dissipation rate are presented in Fig. 13. In the upper layer (200–600 m), the average turbulent dissipation rate inside shallow anticyclones (vertical extent of less than 200 m) increased with the vertical extent of the eddies. When the eddy vertical extent was larger than 250 m, the positive correlation disappeared, and the turbulent dissipation rate ( $\log_{10} \varepsilon$ , W/kg) remained at approximately -9.5. Below 600 m, no significant relationship was observed between the average turbulent dissipation rate inside shallow anticyclones (vertical extent less than 250 m) and the eddy vertical extent. For cyclones, the relationship between the turbulent dissipation rate and the vertical extent was similar throughout the upper 2000 m. The average turbulent dissipation rate inside shallow cyclones (vertical extent less than 300 m) increased with the vertical extent; this positive

correlation disappeared when the vertical extent was greater than 300 m.

Turbulent diffusivity,  $\kappa$ , is another parameter for measuring turbulent mixing. Turbulent diffusivity is defined as  $\kappa = \gamma\epsilon/\overline{N}^2$ , where a mixing efficiency of  $\gamma = 0.2$  is used,  $\epsilon$  is the turbulent dissipation rate, and  $\overline{N}^2$  is the average buoyancy frequency inside the eddies. Therefore, the difference between the turbulent dissipation rate and diffusivity is related to stratification. The relationship between the turbulent diffusivity ( $\log_{10} \kappa$ ) and vertical extent is shown in Fig. 14. The turbulent diffusivity inside shallow anticyclones was much larger than that inside shallow cyclones, indicating that the weak stratification leading to anticyclones was not as stable as that leading to cyclones. Thus, turbulent mixing processes are insensitive to changes in the upper ocean (less than 600 m in depth).

### 3.6 Eddy aspect ratio and turbulent dissipation rate

The eddy aspect ratio is the vertical half-thickness over the radius, which is a three-dimensional index describing the geometric characteristics of eddies. Different eddies are produced and developed in different ways, and the aspect ratios can range from wide and shallow to narrow and deep as latitude increases. In this section, we determine the relationship between the eddy aspect ratio and turbulent dissipation rate to provide a reference value for the turbulent dissipation rate for use in eddy simulations.

The dataset used for this analysis contained 8688 eddies. Because the number of eddies with an aspect ratio greater than 0.015 accounted for only 5% of the entire dataset, such eddies were removed to reduce the influence of extreme values. After filtering, 8017 eddies (3924 cyclones and 4093 anticyclones) were retained. The relationship between the eddy aspect ratio and the turbulent dissipation rate is shown in Fig. 15. The magnitude of the average turbulent dissipation rate ( $\log_{10} \epsilon$ , W/kg) inside anticyclones at depths of 200–600 m ranged from -9.9 to -9.6 when the aspect ratio was less than 0.005 and maintained a constant value of -9.6 when the aspect ratio was greater than 0.005. Between 600 and 1000 m, the magnitude of the average turbulent dissipation rate inside anticyclones reached a maximum value. When the aspect ratio was less than 0.008, the magnitude increased from -11.35 to -10.9; when the aspect ratio was greater than 0.008, the magnitude decreased from -10.9 to -11.1. Below 1000 m, the distribution of the magnitude of the average turbulent dissipation rate inside anticyclones was similar to that observed for the 200–600 m depth; when the aspect ratio was greater than 0.005, the magnitude approached -11.7. In contrast, the magnitude of the average turbulent dissipation rate inside cyclones exhibited a uniform distribution between the depth three segments, which was characterized by skewness. As shown in Fig. 15, the magnitude of the average turbulent dissipation rate inside cyclones reached a maximum when the aspect ratio was 0.01.

In summary, the turbulent dissipation rate inside anticyclones was largest when

the aspect ratio was 0.007; the turbulent dissipation rate was positively correlated with the eddy aspect ratio, when the aspect ratio was less than 0.007. The turbulent dissipation rate inside cyclones was largest when the aspect ratio was 0.01 and decreased as the value of the aspect ratio moved away from 0.01 in either direction. The greater the difference between the aspect ratio and the value of 0.01, the smaller the turbulent dissipation rate.

## Summary and conclusions

Based on the parameterized theory of turbulent mixing, the turbulent dissipation rate inside the eddies can be calculated and analyzed using Argo float profiles. This study focused on two major issues: (1) the near-global distribution of the turbulent dissipation rate inside eddies and (2) the relationship between basic morphological characteristics of eddies (such as the radius, vertical extent, and aspect ratio) and the turbulent dissipation rate inside eddies. Using SSHA data combined with Argo float profiles, the spatial and seasonal distribution of turbulent dissipation rates inside eddies for segments centered at depths of 200–600 m, 600–1000 m, and 1000–2000 m was investigated. The results demonstrated that heightened mixing occurs in the ACC and WBC regions, such as the Kuroshio and Gulf streams, which are also regions of active mesoscale eddies with high mesoscale kinetic energy. In addition, the seasonal characteristics of the dissipation rate inside the eddies only existed in the upper layer (200–600 m) and indicated that the turbulent dissipation rates in winter and spring are generally larger than those in summer and autumn.

The relationship between eddy characteristics and turbulent mixing was investigated in detail. According to our analysis, the turbulent dissipation rate inside anticyclones was larger than that inside cyclones. In addition, turbulent mixing at the eddy center was enhanced, regardless of eddy polarity; however, while the distribution of turbulent dissipation rates was uniform inside the remaining areas of cyclones (normalized radius larger than 0.2), turbulent dissipation rates inside anticyclones increased with distance from the eddy center.

The turbulent dissipation rates are independent of the horizontal scale of eddies but are related to the vertical extent of eddies. According to our analysis, turbulent dissipation rates inside shallow eddies (with vertical extent less than 250 m for cyclones and 300 m for anticyclones) usually increased with the vertical extent of the eddies; however, for shallow anticyclones, this positive correlation faded when the depth exceeded 600 m. We also assessed the relationship between eddy aspect ratio and turbulent dissipation rates and found that, for cyclones, the closer the aspect ratio was to 0.01, the larger the turbulent dissipation rate was. With regards to anticyclones, the turbulent dissipation rate was largest when the aspect ratio was 0.007 and decreased as the aspect ratio decreased.

In conclusion, the results presented herein may provide a reference for turbulence parametrization schemes. The relationships we discovered between eddy

feathers and the turbulent dissipation rate will enhance our understanding of the dynamic processes occurring inside eddies.

### **Acknowledgements**

This study was supported by National Nature Science Foundation of China (Grant No.42076015), and the National Key Research and Development Program of China (Grant Nos.2017YFA0604104). We thank Wiley (<https://wileyeditingservices.com/en/>) for its linguistic assistance during the revision of this manuscript.

## **Reference**

Adams K A., Hosegood P., Taylor J R., et al. Frontal Circulation and Submesoscale Variability during the Formation of a Southern Ocean Mesoscale Eddy. *Journal of Physical Oceanography*, 2017, 47(7):1737-1753.

Aubert O, Le Bars M, Le Gal P, et al. The Universal Aspect Ratio of Vortices in Rotating Stratified Flows: Experiments and Observations. *Journal of Fluid Mechanics*, 2012, 706:34-4.

Cairns J L, Williams G O. Internal wave observations from a midwater float. *Journal of Geophysical Research*, 1976, 81(12): 1943-1950.

Carter G S, Gregg M. C. Intense, Variable Mixing near the Head of Monterey Submarine Canyon. *Journal of Physical Oceanography*, 2002, 32(11):3145-3165.

Caulfield, C, P, et al. Role of overturns in optimal mixing in stratified mixing layers. *Journal of Fluid Mechanics*, 2017.

Chaigneau A, Pizarro O, Rojas W. Global climatology of near-inertial current characteristics from Lagrangian observations. *Geophysical Research Letters*, 2008, 35(13).

Chang Y L, Miyazawa Y, Guo X. Effects of the STCC eddies on the Kuroshio based on the 20-year JCOPE2 reanalysis results. *Progress in Oceanography*, 2015, 135: 64-76.

Charney J G. Geostrophic turbulence. *Journal of the Atmospheric Sciences*, 1971, 28(6): 1087-1095.

Chelton D B, Schlax M G, Samelson R M, et al. Global observations of large oceanic eddies. *Geophysical Research Letters*, 2007, 34(15).

Chelton D B, Schlax M G, Samelson R M. Global observations of nonlinear mesoscale eddies. *Progress in Oceanography*, 2011, 91(2):167-2.

- Doglioli A M, Blanke B, Speich S, et al. Tracking coherent structures in a regional ocean model with wavelet analysis: Application to Cape Basin eddies. *Journal of Geophysical Research: Oceans*, 2007, 112(C5).
- Dong C, Nencioli F, Liu Y, et al. An automated approach to detect oceanic eddies from satellite remotely sensed sea surface temperature data. *IEEE-Geoscience and Remote Sensing Letters*, 2011, 8(6):
- Egbert G D, Ray R D. Semi-diurnal and diurnal tidal dissipation from TOPEX/Poseidon altimetry. *Geophysical Research Letters*, 2003, 30(17).
- Faghmous J H, Frenger I, Yao Y, et al. A daily global mesoscale ocean eddy dataset from satellite altimetry. *Scientific Data*, 2015,
- Garrett C, Munk W. Space-time scales of internal waves: A progress report. *Journal of Geophysical Research*, 1975, 80(3): 291-297.
- Gregg M. C. Diapycnal mixing in the thermocline: A review, *Journal of Geophysical Research: Oceans* (1978-2012), 1987, 92(C5): 9686-9698.
- Gregg M C, Sanford T B, Winkel D P. Reduced mixing from the breaking of internal waves in equatorial waters. *Nature*, 2003, 422(6931): 513-515.
- Gregg M C. Scaling turbulent dissipation in the thermocline. *Journal of Geophysical Research: Oceans*, 1989, 94(C7): 9686-9698.
- Guo, M., Chen, R., Xu, H., and Vetter, P. A. Dynamical features of near-inertial motions in global ocean based on the gdp dataset from 2000 to 2019. *Acta Oceanologica Sinica*, 2012, 39(12).
- Hassanzadeh, P., Marcus, P. S. & Le Gal, P. The universal aspect ratio of vortices in rotating stratified flows: theory and simulation. *Fluid Mech*, 2012, 706, 46-47.
- HE Jingjing, LIN Xiaopei. Co-variation of the surface wind speed and the sea surface temperature over mesoscale eddies in the Gulf Stream region: momentum vertical mixing aspect. *Journal of Oceanology and Limnology*, 2019, 37(04): 1154-1164.
- Kunze E, Sanford T B. Abyssal Mixing: Where It Is Not. *J. phys. oceanogr*, 2009, 26(10): 2286-2296.
- Kunze E, Firing E, Hummon J M, et al. Global Abyssal Mixing Inferred from Lowered ADCP Shear and CTD Strain Profiles. *Journal of Physical Oceanography*, 2006, 36(8): 1553-157.
- Liao G, Xu X, Dong C, et al. Three-Dimensional Baroclinic Eddies in the Ocean: Evolution, Propagation, Overall Structures, and Angular Models. *Journal of Physical Oceanography*, 2019, 49(10): 2571-2599

- Lilly J M, Scott R K, Olhede S C. Extracting waves and vortices from Lagrangian trajectories. *Geophysical Research Letters*, 2011, 38(23).
- Liu ZhiYing, Liao Guang Hong, Hu Xiao Kai, Zhou Bei Feng (2020). Aspect ratio of eddies inferred from argo floats and satellite altimeter data in the ocean. *Journal of Geophysical Research: Oceans*, 125(1).
- Meyer A, Phillips H E, Sloyan B M, et al. Mixing (MX) Oceanographic Toolbox for EM-APEX\* float data applying shear-strain finescale parameterization. 2014.
- Nencioli F, Dong C, Dickey T, et al. A vector geometry-based eddy detection algorithm and its application to a high-resolution numerical model product and high-frequency radar surface velocities in the Southern California Bight. *Journal of atmospheric and oceanic technology*, 2010, 27(3): 564-579.
- Peters H. Observations of Stratified Turbulent Mixing in an Estuary: Neap-to-spring Variations During High River Flow. *Estuarine Coastal & Shelf Science*, 1997, 45(1):69-88.
- Petersen M R, Williams S J, Maltrud M E, et al. A three-dimensional eddy census of a high-resolution global ocean simulation. *Journal of Geophysical Research: Oceans*, 2013, 118(4): 1759-1774.
- Polzin K. L., Toole J. M., Schmitt R. W. Finescale parameterizations of turbulent dissipation, *Nature*, 1996, 380(6569): 54-57.
- Pope V, Stratton R. The processes governing horizontal resolution sensitivity in a climate model. *Climate Dynamics*, 2002, 19(3-4):211-236.
- Qi Y, Shang C, Mao H, et al. Spatial structure of turbulent mixing of an anticyclonic mesoscale eddy in the northern South China Sea. *Acta Oceanologica Sinica*, 2020, 39(11): 69-81.
- Sheen K L, Brearley J A, Naveira Garabato A C, et al. Modification of turbulent dissipation rates by a deep Southern Ocean eddy. *Geophysical Research Letters*, 2015, 42(9): 3450-3457.
- Souza J, de Boyer Montégut C, Cabanes C, et al. Estimation of the Agulhas ring impacts on meridional heat fluxes and transport using ARGO floats and satellite data. *Geophysical Research Letters*, 2011, 38(21).
- Thorpe S A. *The turbulent ocean*. Cambridge: Cambridge University Press, 2005.
- Vallis G K. *Atmospheric and Oceanic Fluid Dynamics: Fundamentals and Large-scale Circulation*. 2006.
- Wei, Zhao, Lei, et al. The Roles of Kuroshio Intrusion and Mesoscale Eddy in Upper Mixing in the Northern South China Sea. *Journal of Coastal Research: An International Forum for the Littoral Sciences*, 2014.

- Whalen C B , Talley L D , Mackinnon J A . Spatial and temporal variability of global ocean mixing inferred from Argo profiles. *Geophysical Research Letters*, 2012, 39(18).
- Whalen C B , Mackinnon J A , Talley L D . Large-scale impacts of the mesoscale environment on mixing from wind-driven internal waves. *Nature Geoscience*, 2018, 11(11).
- W.H. Munk. Abyssal recipes. *Deep-Sea Res*, 1966, 13 (4), pp, 707-730.
- Wijesekera H W , Dillon T M , Padman L . Some statistical and dynamical properties of turbulence in the oceanic pycnocline. *Journal of Geophysical Research Oceans*, 1993, 98(C12):22665-22679.
- Wunsch C, Ferrari R. Vertical mixing, energy, and the general circulation of the oceans[. *Annual Review of Fluid Mechanics*, 2004, 36(1): 281-314.
- Yang Q, Zhou L, Tian J, et al. The Roles of Kuroshio Intrusion and Mesoscale Eddy in Upper Mixing in the Northern South China Sea. *Journal of Coastal Research*, 2014, 30(1):192-198.
- Yang, G.-B., Zheng, Q., Yuan, Y., Zhuang, Z., Hui, Z., Guo, Y.-L., et al. Effect of a mesoscale eddy on surface turbulence at the Kuroshio front in the East China Sea. *Journal of Geophysical Research: Oceans*, 2019, 124, 1763–1777.
- Zhai X, Greatbatch R J, Zhao J. Enhanced vertical propagation of storm-induced near-inertial energy in an eddying ocean channel model. *Geophysical research letters*, 2005, 32(18).

## Figure legends

**Table.1 The quantities of the Argo floats trapped inside an eddy**

The quantities of the Argo floats trapped inside an eddy	The quantities of the cyclones	The quantities of the anticyclones	Total quantities of the eddies
1	207863	206333	414196 (89.76%)
2-20	24056	22859	46915 (10.17%)
21-80	135	211	346 (0.07%)

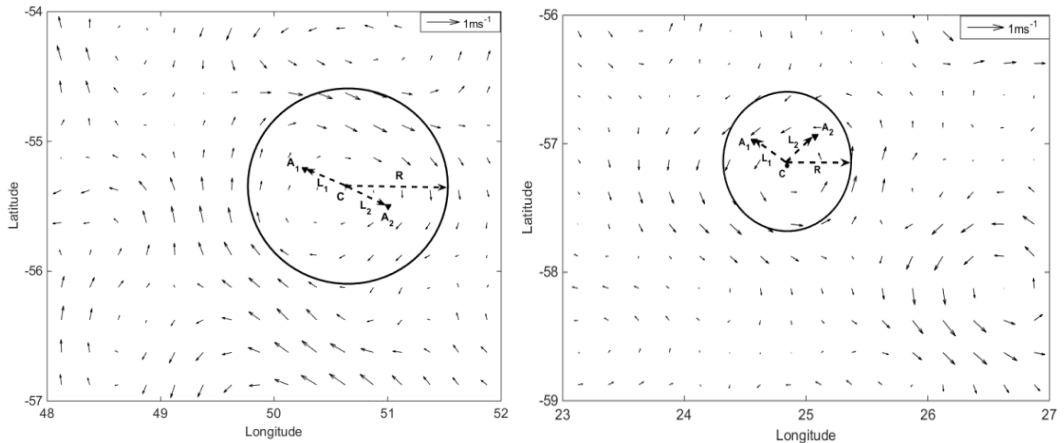


Fig. 1 Rotational symmetry component of the eddies and illustrative examples of the Argo floats collected from the eddies. Left, cyclone; right, anticyclone. F, the position of the Argo floats; C, eddy center.

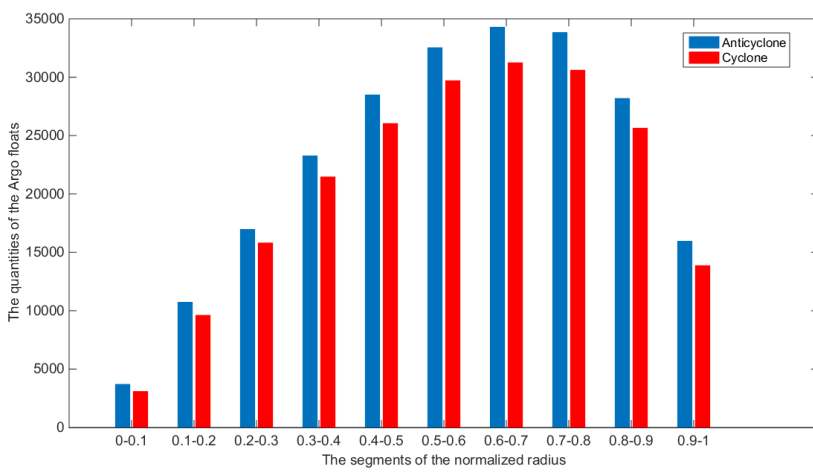


Fig. 2 Histogram of the number of Argo floats inside a normalized eddy.

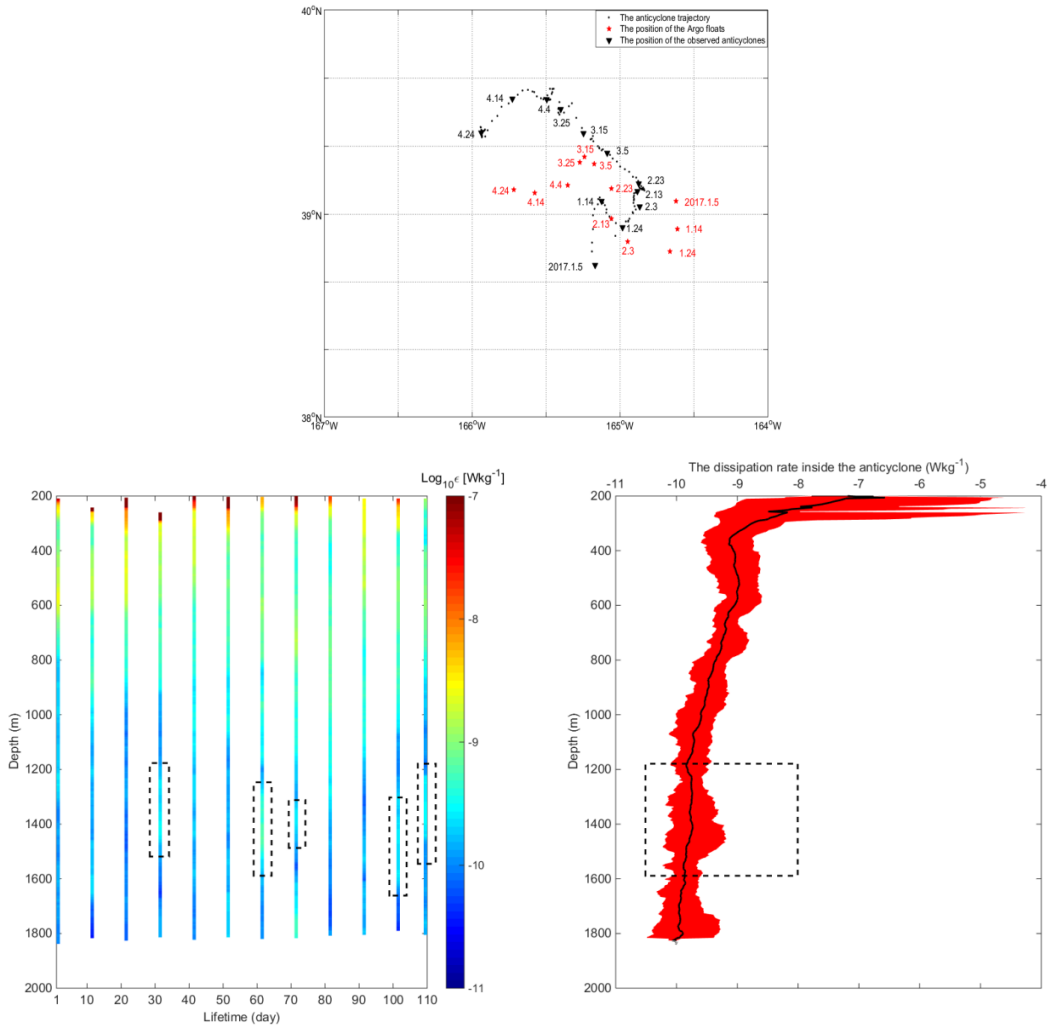


Fig. 3 Example of an anticyclone trajectory to illustrate the variability of the turbulent dissipation rate along the eddy trajectory. (a) Positions of the observation stations and the anticyclone trajectory. (b) Dissipation rate profiles along the anticyclone trajectory. (c) Average turbulent dissipation rate profile.

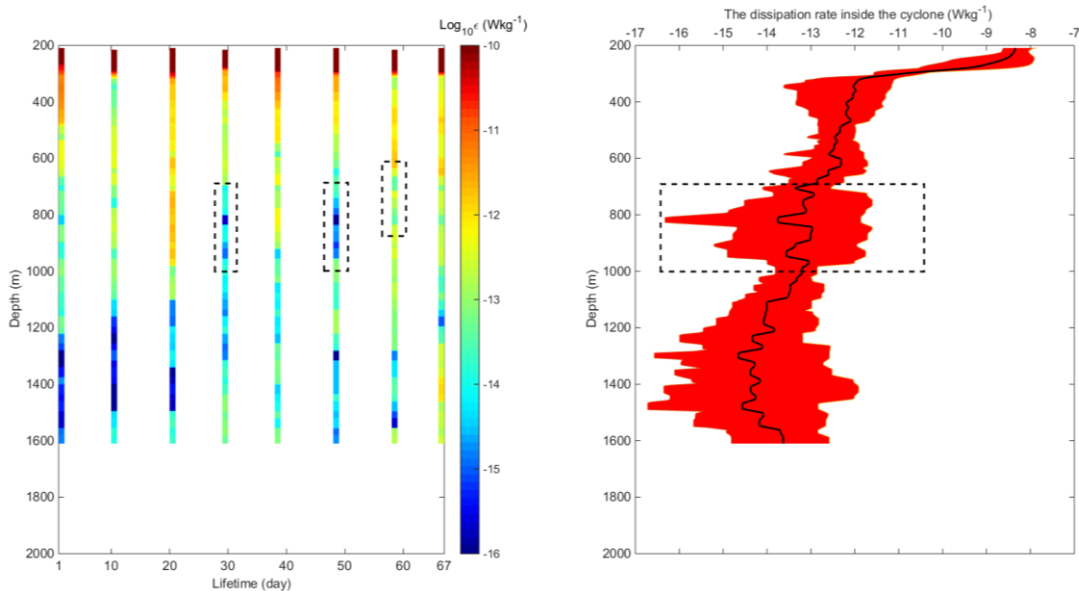
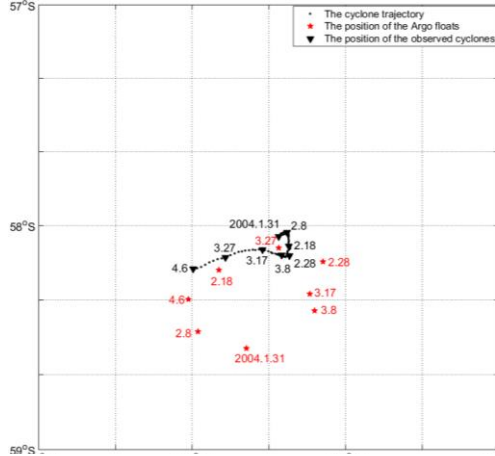


Fig. 4 Example of a cyclone trajectory to illustrate the variability of the turbulent dissipation rate along the eddy trajectory. (a) Positions of the observation stations and the cyclone trajectory. (b) Dissipation rate profiles along the cyclone trajectory. (c) Average turbulent dissipation rate profile.

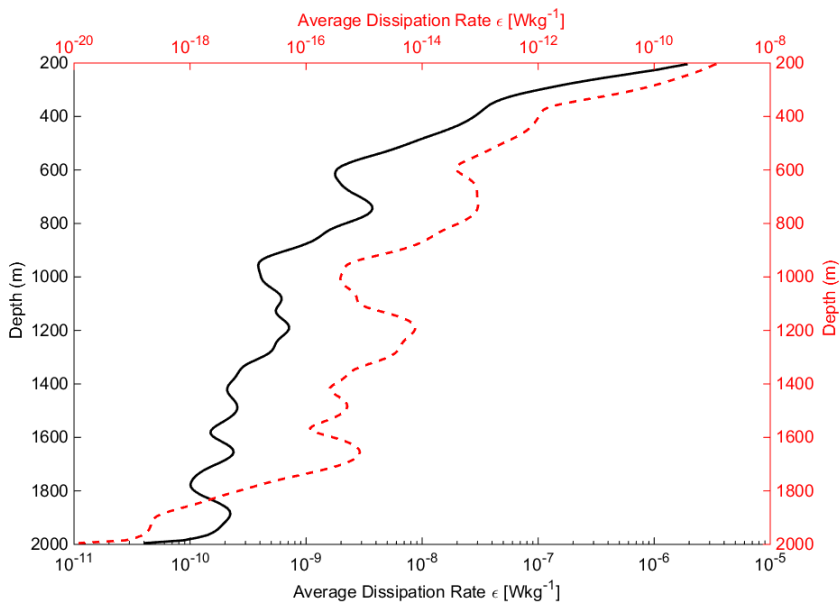


Fig. 5 Vertical profile of the average dissipation rate inside eddies. The red dotted line indicates variance.

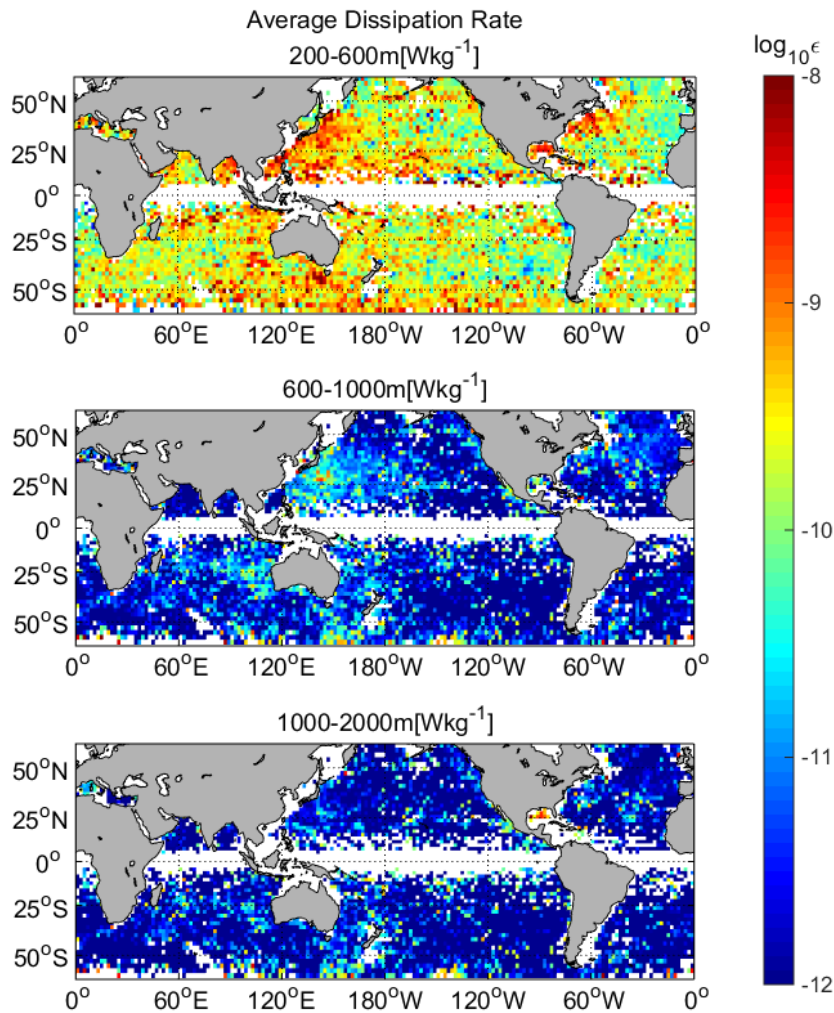


Fig. 6 Spatial distribution of the turbulent dissipation rate inside eddies.

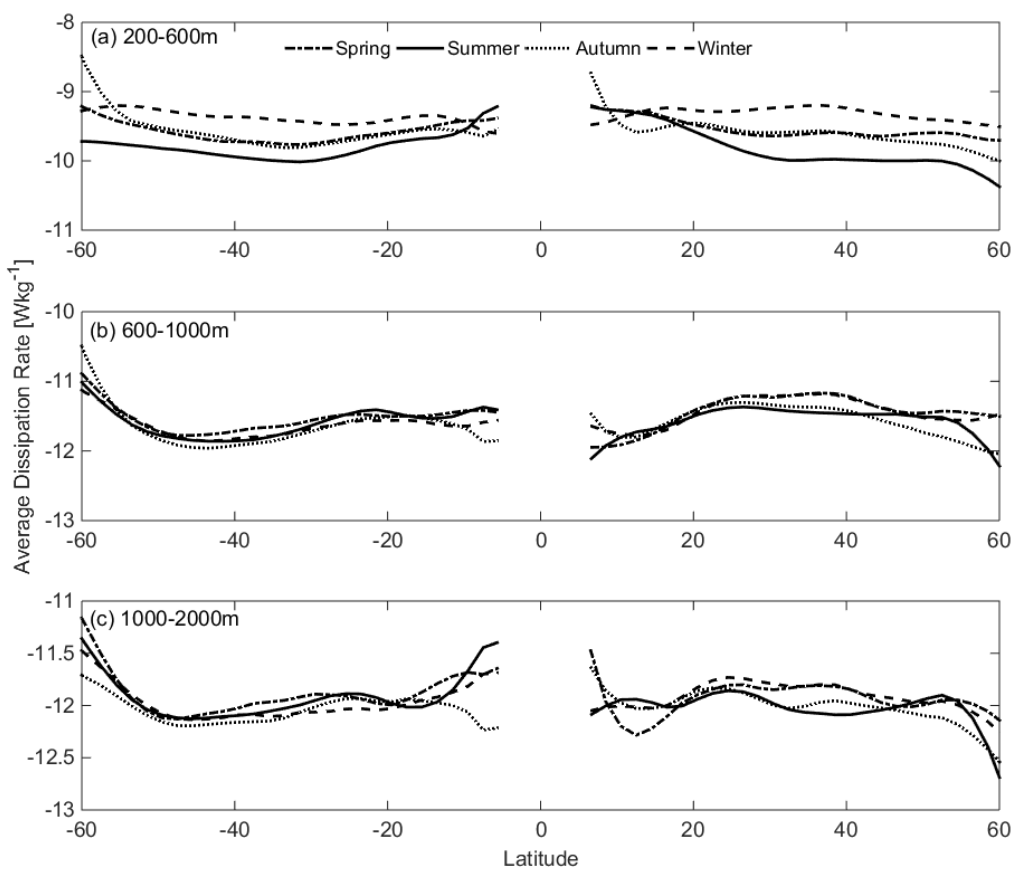


Fig. 7 Seasonal distribution of the turbulent dissipation rate inside eddies.

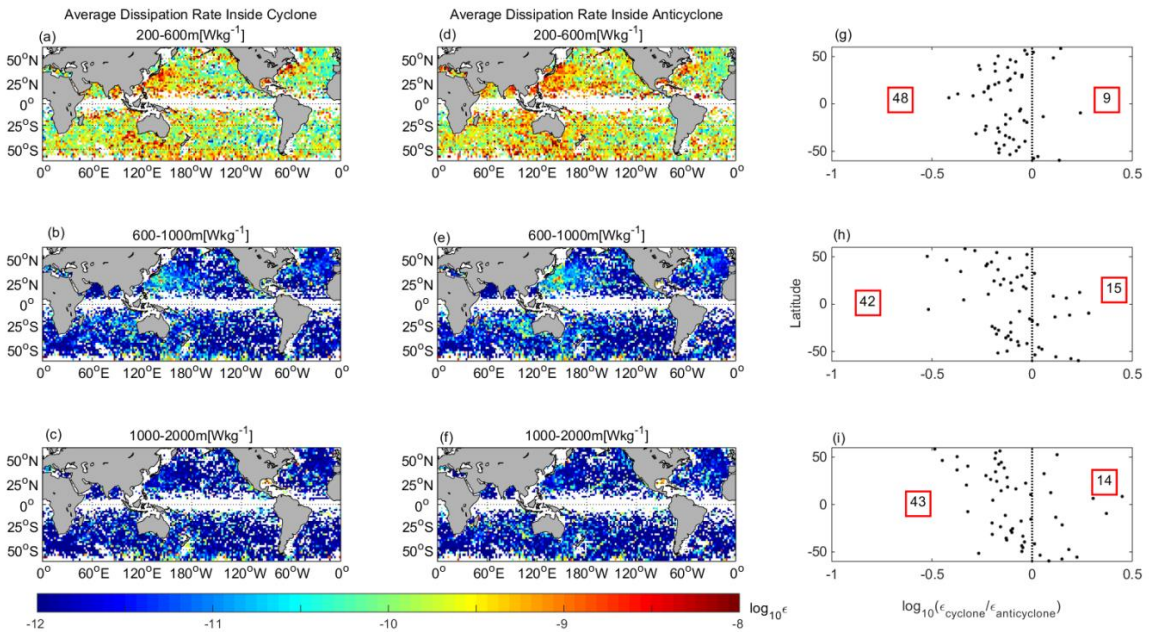


Fig. 8 Comparison of the turbulent dissipation rate inside cyclones and anticyclones.

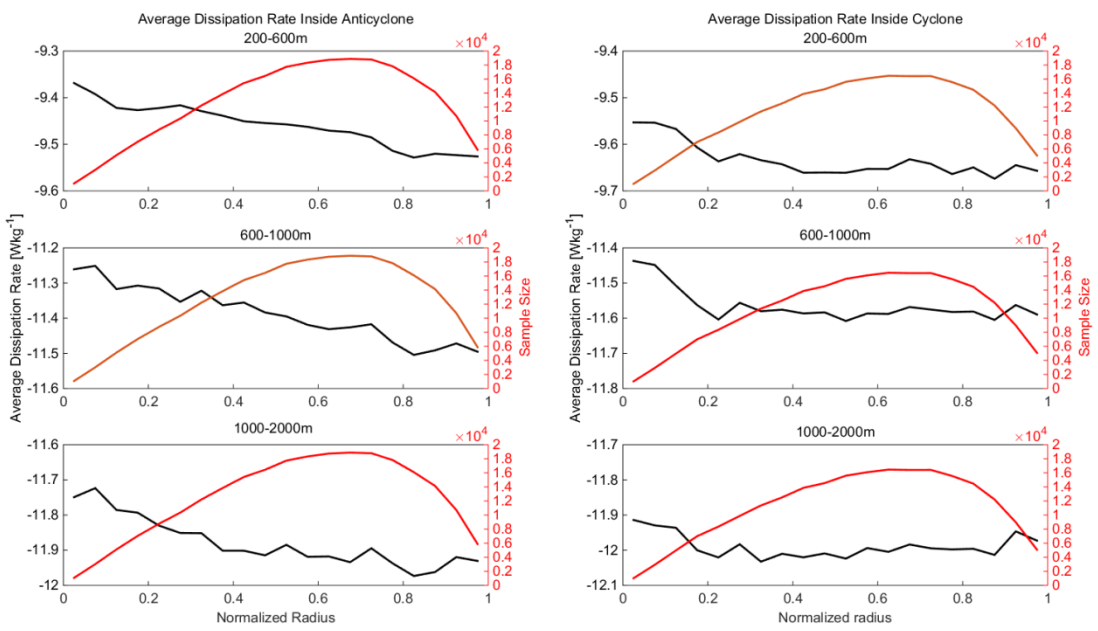


Fig. 9 Relationship between turbulent dissipation rate inside eddies and the normalized eddy radius. The red line indicates the number of samples.

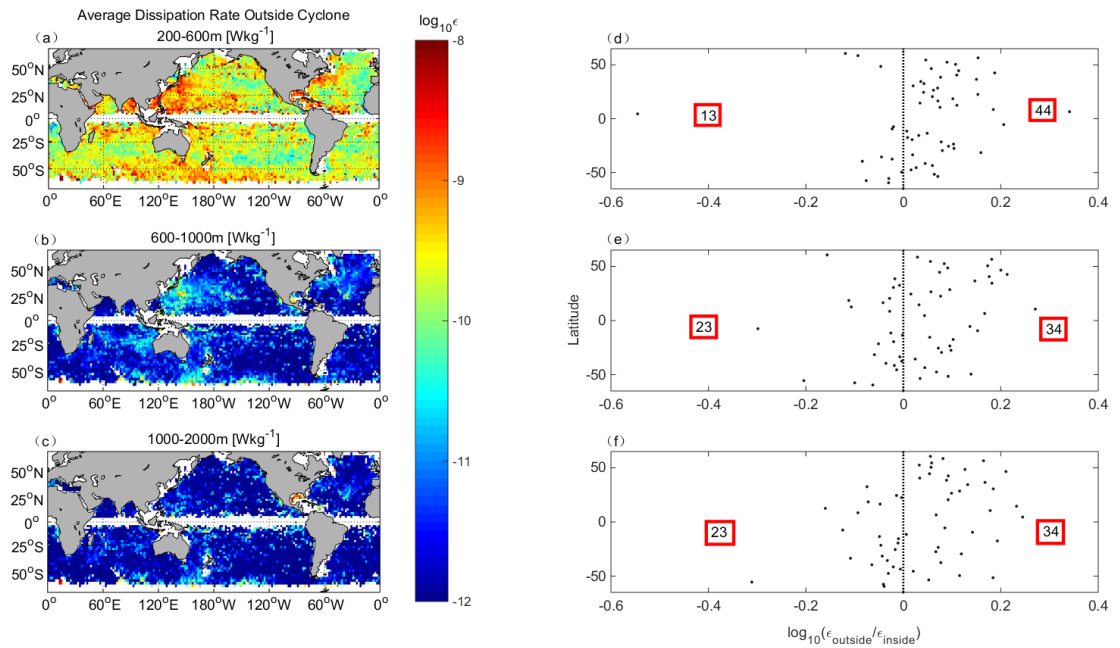


Fig. 10 Comparison of the turbulent dissipation rate inside and outside cyclones.

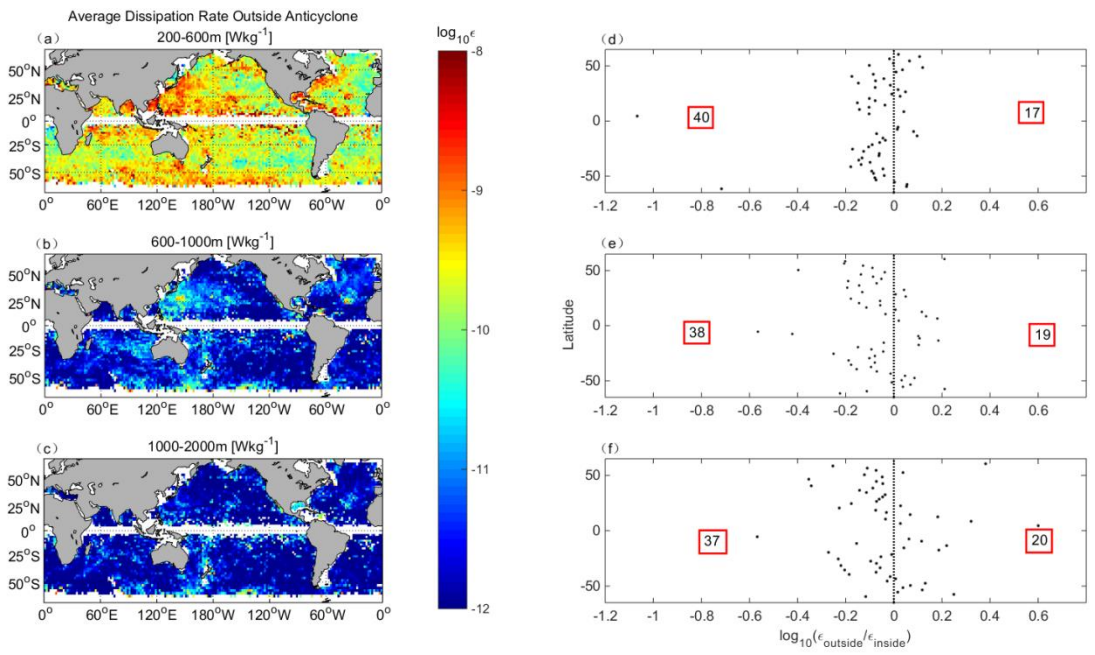


Fig. 11 Comparison of the turbulent dissipation rate inside and outside anticyclones.

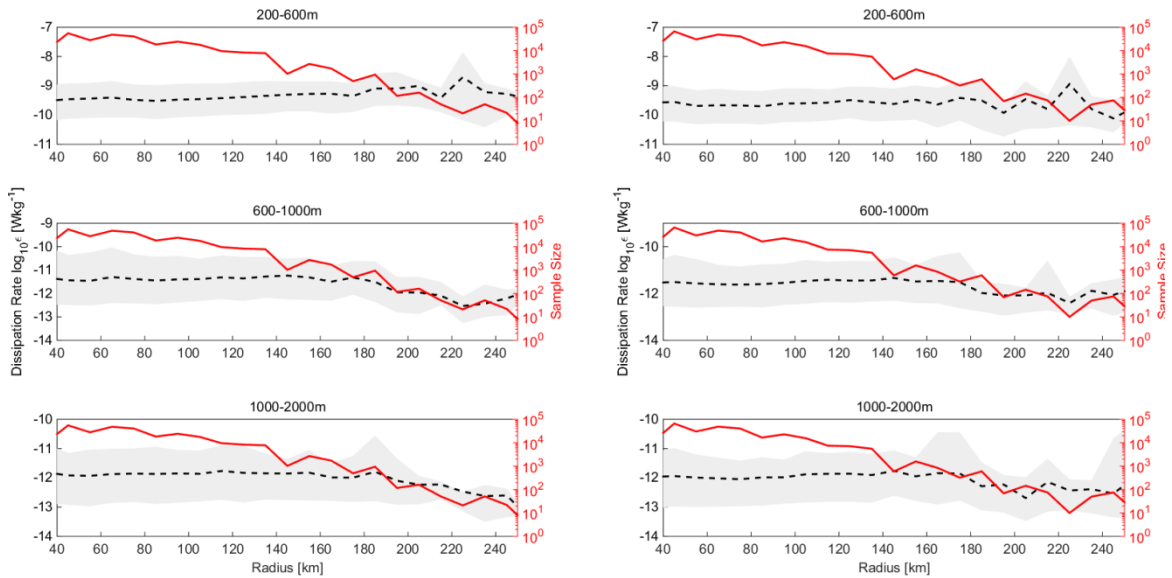


Fig. 12 Relationship between the turbulent dissipation rate inside eddies and the eddy radius. Left, cyclones; right, anticyclones. The red line indicates the number of samples.

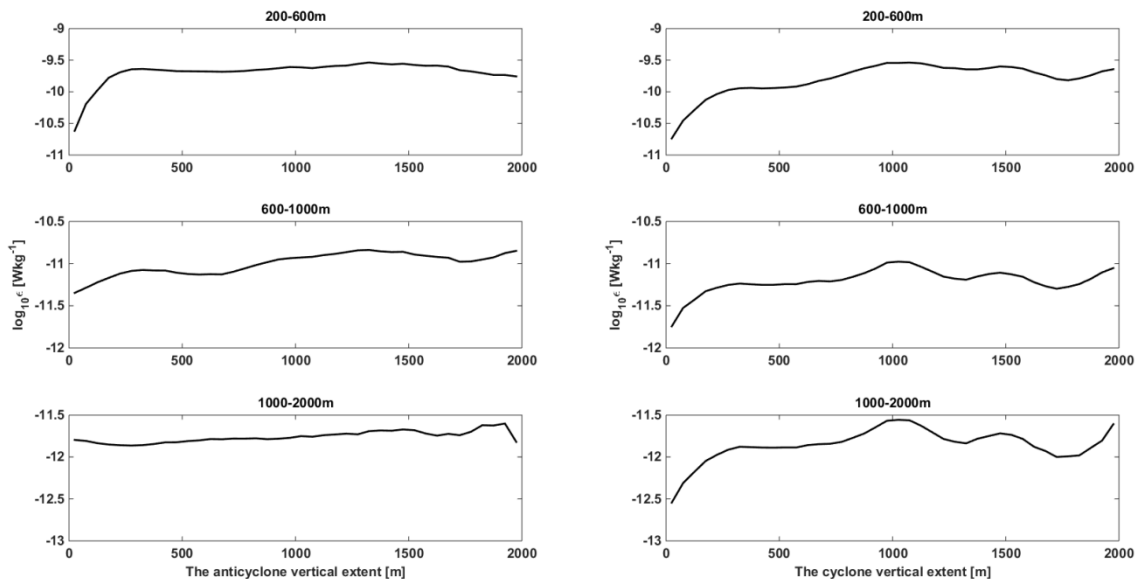


Fig. 13 Relationship between the turbulent dissipation rate inside eddies and the eddy vertical extent. Left, anticyclones; right, cyclones.

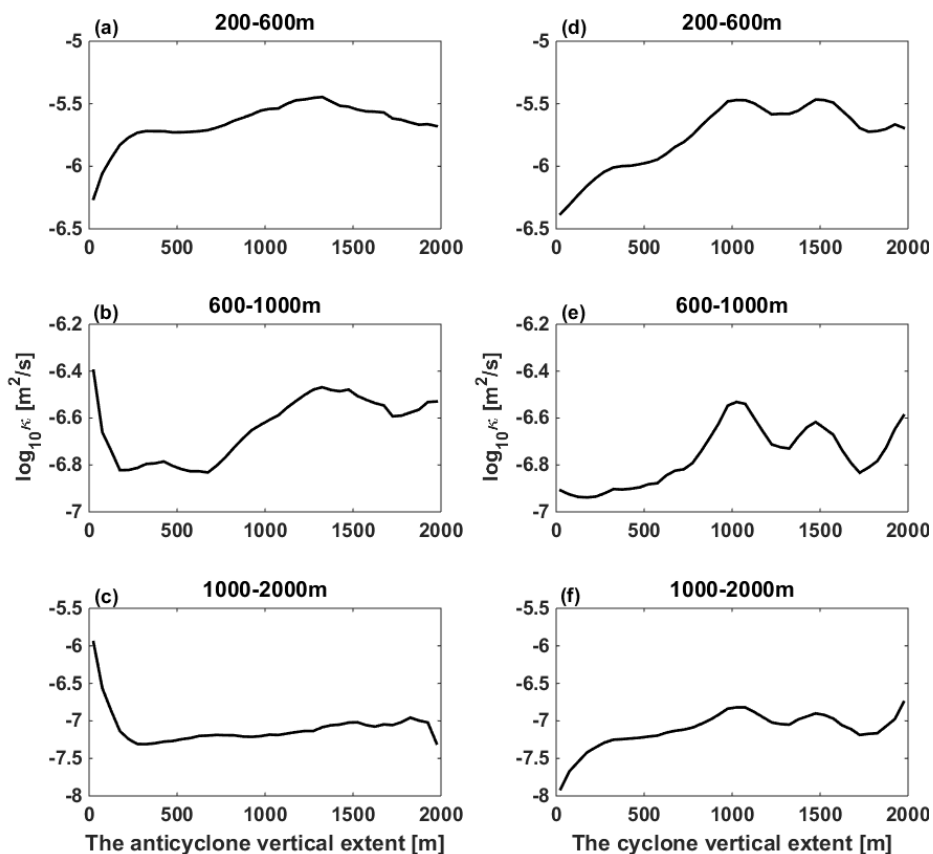
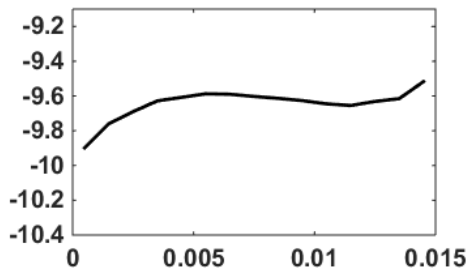
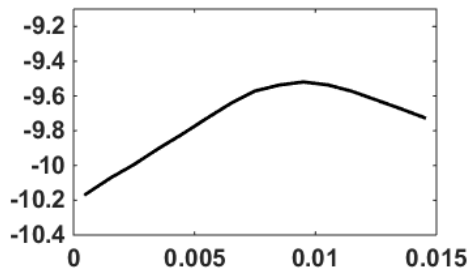
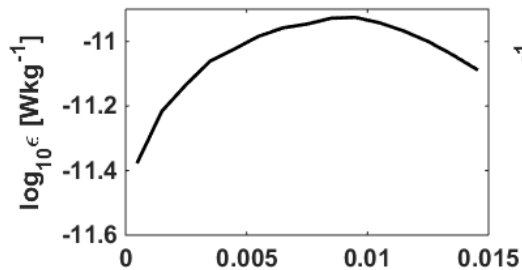
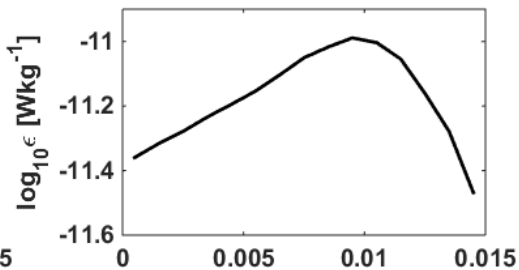
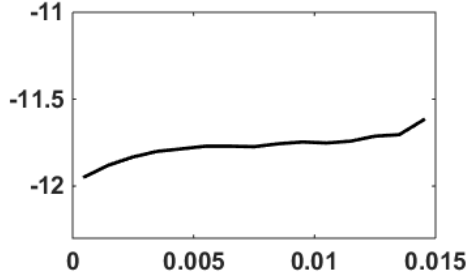
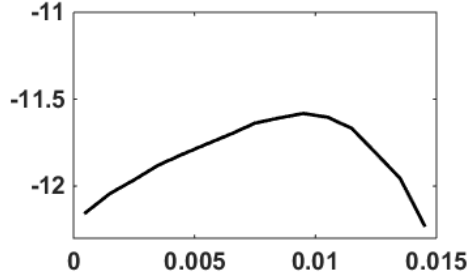


Fig. 14 Relationship between the turbulent diffusivity inside eddies and the eddy vertical extent. Left, anticyclones; right, cyclones.

**200-600m****200-600m****600-1000m****600-1000m****1000-2000m****1000-2000m**

The anticyclone aspect ratio

The cyclone aspect ratio

Fig. 15 Relationship between the turbulent dissipation rate inside eddies and the eddy aspect ratio. Left, anticyclones; right, cyclones.